Photoacoustic and Optical spectral transformations in Solid Lipid Nanoparticles labelled with increasing concentrations of Photoacoustic NIR BODIPY †

Clément Linger,[a,b] Giulia Maccini,[a] Gilles Clavier,[c] Rachel Méallet,[d] Nicolas Tsapis,‡*[a] and Jérôme Gateau ‡*[b]

Solid lipid nanoparticles labelled with a photoacoustic BODIPY dye exhibit complex but continuous transformation for both optical and photoacoustic spectra as the BODIPY content increases. Gaussian decomposition of the spectra reveals the interplay between three optical absorption bands and unveils a band-dependent and concentration-dependant photoacoustic generation efficiency above 1.

Solid Lipid Nanoparticles (SLNs) are increasingly studied for therapeutic applications because of their ability to deliver mostly hydrophobic drugs[1]. They are also promising theranostic agents with the co-encapsulation of imaging contrast agents, and have already been used for image-guided therapy with MRI[2,3]. Investigations for optical imaging are just emerging, with at least one study[4] in which hydrophobic methine dyes were encapsulated in SLNs for fluorescence imaging. Fluorescence and photoacoustic imaging (PAI) are the main optical bioimaging modalities for applications at centimetre depth[5]. We present here the first SLNs developed for PAI. Among the diversity of nanoparticles developed for deep-tissue PAI[6], SLNs combine a great affinity for lipophilic dyes for a high dye loading, and a lipid core with excellent thermoelastic efficiency[7] (Grüneisen coefficient) for photoacoustic generation.

We focus here on SLNs co-encapsulating a drug and a near infrared (NIR) absorbing dye designed for PAI. The chosen formulation process[8] remarkably enables to tune the optical label concentration per particle up to being the major component of the system. We investigate the optical and photoacoustic (PA) spectral properties as the label concentration increases.

PAI is based on the transformation of optically absorbed energy into ultrasound, through photothermal conversion and thermo-elastic expansion[9]. The ultrasound signal is proportional to the absorbed energy converted into heat, which calls for a high photothermal conversion efficiency (PTCE) and a large absorption cross section in the NIR range (optical window of biological tissues typically between 650 and 1300 nm). As for the absorption spectrum, NIR dyes are attractive contrast agents because of the presence of absorption bands which provide a spectral signature different from the ones of haemoglobin[6]. However, it has recently been shown that the PA generation at different wavelengths can significantly differ from the optical absorption spectrum for dyes and dye aggregates[10], because of the wavelength-dependent PTCE. A quantitative PA characterization of our dye-loaded SLNs was performed with a recently developed and novel calibrated photoacoustic spectrometer[11]. This PA spectrometer measures the photoacoustic coefficient θ_{10}^{PA} and its spectral variations:

$$\theta_{10}^{PA}(\lambda) = PGE(\lambda).\mu_{a,10}(\lambda) \quad (1)$$

where λ is the optical wavelength, $\mu_{a,10}(\lambda)$ is the decadic absorption coefficient and $PGE(\lambda)$ is the photoacoustic generation efficiency. PGE is the product of the PTCE and the thermo-elastic expansion efficiency relative to water[10,11] (cf. ESI).

The SLN formulation is based on dexamethasone palmitate (DXP) and DSPE-PEG_{2000}[8] (Fig. 1(a)). DXP is a prodrug of dexamethasone, an anti-inflammatory drug, released by enzymatic cleavage once administered *in vivo*. The anti-inflammatory activity of DXP SLNs was proved *in vivo* in a murine model of rheumatoid arthritis[8]. For the optical labelling in the NIR, we modified the PA BODIPY dye (BY) initially developed by Bodin *et al*.[12] by grafting a palmitate chain (BY-

[a] *Université Paris-Saclay, CNRS, Institut Galien Paris-Saclay, 91400 Orsay, France.*
[b] *Sorbonne Université, CNRS, INSERM, Laboratoire d'Imagerie Biomédicale, 75006 Paris, France.*
[c] Université Paris-Saclay, ENS Paris-Saclay, CNRS, PPSM, 91190 Gif-sur-Yvette, France.
[d] *Université Paris-Saclay, CNRS, Institut des Sciences Moléculaires d'Orsay, 91405 Orsay, France.*
* Correspondence: jerome.gateau@sorbonne-universite.fr and nicolas.tsapis@universite-paris-saclay.fr
‡ Equal leading contribution.
† Electronic Supplementary Information (ESI) available:

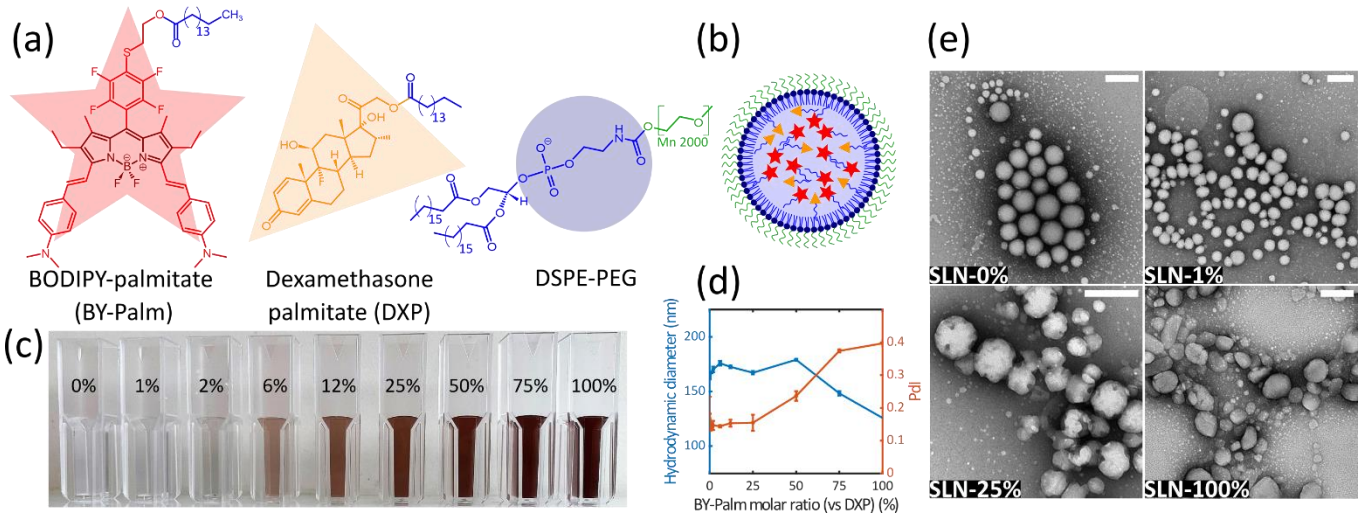

Fig. 1 – (a) Molecules involved in the solid lipid nanoparticle (SLN) formulation with their schematic representations. (b) Supposed structure of the SLN using schematic representation: red star for BODIPY, yellow triangle for dexamethasone, blue circle for phosphatidylcholine head of DSPE-PEG, blue line for lipidic chain and green line for PEG chain. (c) Picture of the BY-Palm concentration ladder created by the 9 SLN formulations (percentages referring to the molar proportion of BY-Palm versus DXP). Each sample is a 50-fold dilution of formulation result. (d) SLN hydrodynamic diameter measured by dynamic light scattering (left y-axis) and SLN polydispersity index (PdI, right y-axis) as a function of the molar ratio of BY-Palm versus DXP. Mean values and error bars (standard deviation) of triplicate measurements. (e) SLN TEM images with negative staining (uranyl acetate 2% w/w) obtained with JEOL JEM-1400 microscope at an acceleration voltage of 120 kV. Magnifications for SLN-0%, SLN-1%, SLN-25% and SLN-100% are 15,000, 12,000, 25,000 and 15000, respectively. White scale bars on the top right corner represent 200 nm.

Palm, Fig. 1(a)). Lipid grafting was performed through esterification of an alcohol function with a palmitoyl chloride. Chemical grafting prevents dye leakage from the SLNs and limits burst release. Moreover, BY-Palm has a palmitate chain similarly to DXP, suggesting the possibility of formulation into SLNs without DXP. BY has a high molar extinction coefficient at 753 nm (80,000 $L \cdot mol^{-1} \cdot cm^{-1}$), and does not exhibit significant cytotoxicity. BY was selected over the widespread but amphiphilic heptamethine cyanine dyes[6], such as indocyanine green, for its hydrophobicity and its photostability[12]. In a previous study[12], BY was grafted to polylactide (PLA) and BY-PLA was formulated into polymeric nanoparticles with PLA–PEG_{5000}. Varying the BY-PLA concentration, the molar absorption coefficient of the nanoparticles increased linearly with the number of BY-PLA per particle. However, the long chain length of PLA (15,000 $g.mol^{-1}$) compared to BY (790 $g.mol^{-1}$) limited the actual dye loading to 2.9% (w/w). BY-Palm has much lower molecular weight (1,029 $g.mol^{-1}$) than BY-PLA and a much greater loading of dye is expected in particles with similar diameters (~100-150 nm). One main question therefore arises: how will the optical absorption, the PA properties and the corresponding PGE be impacted by the increasing percentage of dye in the nanoparticle? We can expect the evolution to be more complex than a linear increase.

Dye loading was investigated in a large range by varying the molar ratio (see ESI) of BY-Palm and DXP, up to completely replace the prodrug by the dye. Nine molar percentages of BY-Palm compared to DXP were formulated: SLN-0%, SLN-1%, SLN-2%, SLN-6%, SLN-12%, SLN-25%, SLN-50%, SLN-75% and SLN-100%. All nanoparticles were prepared simultaneously. Because of its simplicity and high reproducibility , the SLN formulation of Lorscheider *et al.*[8] was adapted. Briefly, 12.5 mg of DSPE-PEG_{2000} and 25 mg of the mix of BY-Palm and DXP were dissolved in 2 mL of chloroform. This organic phase was then poured into 5 mL of 4°C Milli-Q water and vortexed for 30 s. After a 2-min and 40%-amplitude sonication, the organic phase was evaporated at ambient temperature under a chemical hood. Nanoparticles were then stored at 4°C. Evaporation at room temperature, instead of rotary evaporator[8], ensures similar conditions of slower evaporation for each batch. Fig. 1(c) shows the nine suspensions that appear darker as the BY-Palm percentage increases.

Interestingly, we succeeded in formulating SLN batches with up to 100% BY-Palm. In absence of the prodrug, SLN-100% can be considered purely as contrast agents. From the application perspective, for percentages above 50% the SLNs can be considered as dominantly contrast agents while below 50% they are dominantly drug carriers. Each batch was characterized by zeta potential, dynamic light scattering (DLS) and transmission electron microscopy (TEM). Characteristics of SLN-0% (without BY-Palm) perfectly match those reported by Lorscheider *et al.*[8]. For other SLN batches, zeta potential was found negative (Fig. S6) with values slightly increasing with the BY-Palm content from -58 mV for SLN-0% to -45 mV for SLN-100%, suggesting a stability by electrostatic and steric repulsions of all SLN suspensions. The hydrodynamic diameter determined by DLS (Fig. 1(d)) is stable ~170 nm for BY-Palm percentage up to 50% and then decreases down to 125 nm for SLN-100%. The polydispersity index (Fig. 1(d)) is below 0.2 for BY-Palm percentage up to 25% and then increases to reach 0.39 for SLN-100%. The stability over time was assessed with DLS measurements: all the batches were stable for at least one month when stored at 4°C and for at least 4 days at 37°C. TEM images in Fig. 1(e) show quite monodisperse spherical particles for SLN-0% and SLN-1% (small dots are DSPE-PEG_{2000} micelles). However, the SLNs become variable in shape and size as BY-Palm percentage increases. The increase of polydispersity is confirmed by TEM with smaller egg-shaped particles for SLN-100%.

Optical properties of SLN batches were characterized by absorbance spectrophotometry and PA spectrometry. To avoid potential bias due to the increasing absorption with the BY-Palm

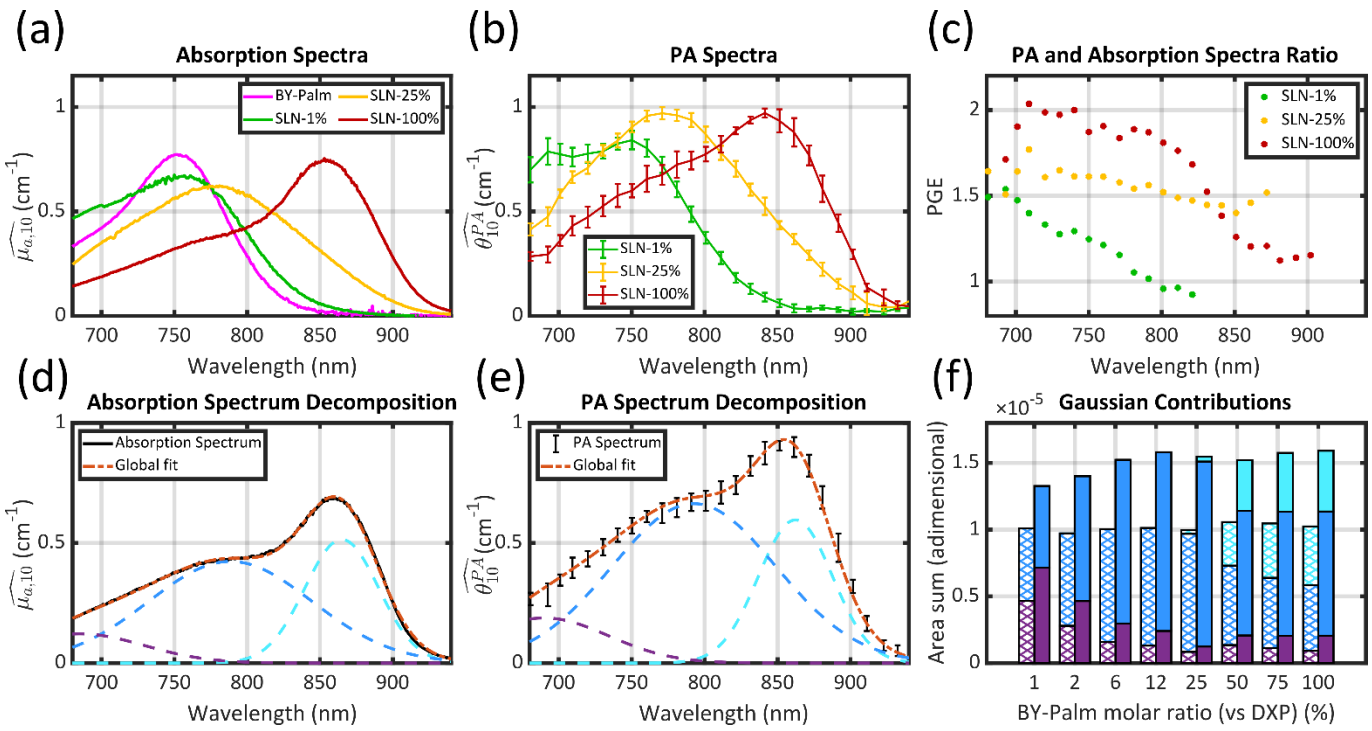

Fig. 2 – (a) Absorption spectra of 3 nanoparticles SLN-1%, SLN-25%, SLN-100%. The absorption spectrum of BY-Palm is also presented in chloroform and with arbitrary units. (b) PA spectra of SLN-1%, SLN-25%, SLN-100%. (c) PA coefficient and absorption ratio for each PA wavelength: Photoacoustic Generation Efficiency (PGE) (d-e) Decomposition of the absorption spectrum (and PA spectrum respectively) for SLN-75% in the sum of three Gaussian functions. From left to right, the Gaussian functions are centred at 685 nm (purple), 788 nm (blue) and 865 nm (cyan). (f) Contribution of each Gaussian function (area) in the total spectrum area for each SLN. Absorption spectra are on the left-hand side in hatched bars while PA spectra are on the right-hand side in coloured bars. The colour code is the same as in (d) and (e).

concentration in SLN suspensions, all batches were diluted in Milli-Q water to obtain solutions with a constant BY-Palm concentration (1.73×10^{-2} mmol.L^{-1}). The same diluted solutions were used to obtain the decadic absorption coefficient $\widehat{\mu_{a,10}}$ and the PA coefficient $\widehat{\theta_{10}^{PA}}$. The hat over the coefficient symbols indicates that the quantities are measured at the defined BY-Palm concentration. Eqn (1) remains valid for the hat metrics with the same PGE. Decadic absorption coefficients (absorbance divided by the length of the cuvette) were acquired with a spectrophotometer equipped with an integrating sphere and SLN-0% were used as blank to limit the influence of the scattering on the absorption spectra (Fig. S4). $\widehat{\mu_{a,10}}$ spectra (Fig. 2(a)) reveal a progressive modification of the photophysical behaviour with the increasing percentage of BY-Palm. For SLN-1%, the spectrum is similar to that of BY-Palm in solution (absorption band around 753 nm). As the BY-Palm percentage increases (Fig. S9), the absorption band shifts gradually to larger wavelengths and become more symmetrical until a new absorption band centred around 860 nm appears. The corresponding PA spectra $\widehat{\theta_{10}^{PA}}$ (Fig. 2(b)) display similar bands but also spectral distortions and globally higher values compare to $\widehat{\mu_{a,10}}$. The PGE (eqn (1) and Fig. 2(c)) is globally greater than 1 and maximum at short wavelengths. Moreover, the PGE between 700 nm and 830 nm increases with the BY-Palm percentage. Similarly to dyes in solution[10], Fig. 2(a-c) clearly illustrates the need of a quantitative PA characterization for nanoparticles comprising NIR dyes as the PGE cannot be assumed equal to 1.

To study the spectral variations in greater detail, we decomposed the $\widehat{\mu_{a,10}}$ and $\widehat{\theta_{10}^{PA}}$ spectra in the range 680- 930 nm as the sum of three Gaussian functions[13]. The position and width of the Gaussian functions were jointly optimized for the absorption and PA spectra, while the amplitude was optimized independently (see ESI). Fig. 2(d) and (e) illustrates that the decomposition enables a satisfactory fit of both the absorption and the PA experimental spectra. The quality of the decomposition was verified for all the percentages (Fig. S10 and S11). The Gaussian functions are ordered by increasing centre wavelength and correspond to different transitions. The first Gaussian function (purple) models the shoulder (a priori S_0-S_1 vibronic state transition[14]), which is mostly visible at BY-Palm percentage below 6%. The middle one (blue) is centred around 760-780 nm and could corresponds to S_0-S_1 0-0 electronic excitation[14]. The enlargement and the bathochromic shift of this band is attributed to partial alignment and change in the environment polarity of BY, as DXP is replaced by BY-Palm (see ESI). The last function (cyan) appears only for BY-Palm percentage above 25% and models a new band with a 100-nm bathochromic shift with regards to SLN-1%, likely corresponding to partial J-type aggregation of BY[15]. Since both the amplitude and the width of the Gaussian function varies with the BY-Palm percentage, we chose to display their area (Fig. 2(f)). The first striking observation is that besides the spectral transformation, the total area (sum of the areas for the three Gaussian functions) is constant for the $\widehat{\mu_{a,10}}$ spectra, and constant and 1.5 times higher for the $\widehat{\theta_{10}^{PA}}$ spectra for BY-Palm percentage above 6%. The constant total areas imply a balance between the absorption bands. For $\widehat{\mu_{a,10}}$, the purple band represents around 50% of the total area for SLN-1% and gradually diminishes to reach a plateau around 10% from SLN-12%. The blue band first

increases with the BY-Palm percentage, reaching 90% of the total area for SLN-12%. From SLN-25%, it gradually decreases, while the cyan band increases. For $\widehat{\theta_{10}^{PA}}$, the behaviour is broadly similar, but the blue and purple bands have higher PGE. Since the Gaussian functions have the same width for $\widehat{\mu_{a,10}}$ and $\widehat{\theta_{10}^{PA}}$, the PGE for each band is the ratio of their area. The PGE is almost constant for the purple band and the cyan band, with an average PGE of 1.7 and 1.1 respectively. However, for the blue band, the PGE increases between 1.1 for SLN-1% and 1.9 at SLN-100%. Band-dependent PGE varying with the degree of aggregation of dyes have been reported for PGEs below 1, which corresponds to different photothermal efficiencies (maximum PTCE of 1)[10]. However, we report here the first band-dependent PGE above 1 for an aqueous suspension. A PGE above 1 corresponds to a thermoelastic expansion (subsequent to the photothermal conversion and quantified by the Grüneisen coefficient) more efficient than for water. The Grüneisen coefficient of water is around 0.12 at 25°C while it varies between 0.5 and 1.1 for lipids[7]. Partial thermal confinement in the SLN during the optical excitation is responsible for the combined expansion of the SLN and the surrounding water layers and results in an effective Grüneisen coefficient relative to water (and a PGE) above 1[16]. Then, two different hypotheses can be made. First, a constant effective Grüneisen coefficient higher than 1.9 could be partially compensated by a band-dependent PTCE. But, this implies a global PTCE below 79% (to reach a global PGE of 1.5, the ratio of the total areas). Such low PTCE does not match with the very weak fluorescence signal of the SLNs (Fig. S8). The second hypothesis is a band-dependent effective Grüneisen coefficient, which implies that the thermal transfer at nanometric scale during the optical pulse excitation (~ 6 ns) leads to enhanced thermal confinement in the lipid core for the blue band, and larger thermal conduction towards the water layer for the purple and cyan bands. Preliminary Cryo-TEM images of SLN-100% suggest an organization of the BY-Palm at nm-scale (see ESI – Fig. S7). However, further investigations will be needed to understand the thermal transfer at nm scale for the different transitions.

We have successfully labelled solid lipid nanoparticles with a BODIPY for PAI, using a simple and direct one-pot formulation protocol. Our particle design enabled to study the absorption and PA spectral transformation with the percentage of dyes incorporated in the SLN. The evolution of the spectral amplitude was not linear with the percentage of dye, but we observed transformations that were quantitatively analysed as a balance between three different bands. Additionally, the fundamental result of a band-dependent photoacoustic generation efficiency above 1 is a new observation that opens the way to careful consideration of the optical and photothermal phenomena at stake in optically labelled nanoparticles for photoacoustic imaging, in particular when constituting materials, such as lipids, possess a Grüneisen coefficient larger than water.

Conflicts of interest

There are no conflicts to declare.

Acknowledgements

This project has received financial support from the French National Research Agency under the program ANR-21-CE09-0024-01 and from the CNRS through the MITI interdisciplinary programs. It has also benefited from Imagerie-Gif core facility supported by l'Agence Nationale de la Recherche (ANR-11-EQPX-0029/Morphoscope, ANR-10-INBS-04/FranceBioImaging; ANR-11-IDEX-0003-02/ Saclay Plant Sciences), with the help of C. Gillet and C. Boulogne. The authors warmly thank F. Gobeaux from LIONS-NIMBE UMR 3685 CEA/CNRS for the cryo-TEM images. This work was supported in part by France Life Imaging under Grant ANR-11-INBS-0006. RM thanks the Région Ile-de-France and DIM NanoK for financial support as well as CHARMMMAT LabEx (11-LABX-0039).

Notes and references

1 J. Akbari, M. Saeedi, F. Ahmadi, S. M. H. Hashemi, A. Babaei, S. Yaddollahi, S. S. Rostamkalaei, K. Asare-Addo and A. Nokhodchi, *Pharm. Dev. Technol.*, 2022, **27**, 525–544.
2 K. Oumzil, M. A. Ramin, C. Lorenzato, A. Hémadou, J. Laroche, M. J. Jacobin-Valat, S. Mornet, C.-E. Roy, T. Kauss, K. Gaudin, G. Clofent-Sanchez and P. Barthélémy, *Bioconjug. Chem.*, 2016, **27**, 569–575.
3 E. Andreozzi, P. Wang, A. Valenzuela, C. Tu, F. Gorin, M. Dhenain and A. Louie, *Bioconjug. Chem.*, 2013, **24**, 1455–1467.
4 G. Chinigò, A. Gonzalez-Paredes, A. Gilardino, N. Barbero, C. Barolo, P. Gasco, A. Fiorio Pla and S. Visentin, *Spectrochim. Acta A Mol. Biomol. Spectrosc.*, 2022, **271**, 120909.
5 V. Ntziachristos, *Nat. Methods*, 2010, **7**, 603–614.
6 J. Weber, P. C. Beard and S. E. Bohndiek, *Nat. Methods*, 2016, **13**, 639–650.
7 S. Liang, B. Lashkari, S. S. S. Choi, V. Ntziachristos and A. Mandelis, *Photoacoustics*, 2018, **11**, 56–64.
8 M. Lorscheider, N. Tsapis, M. ur-Rehman, F. Gaudin, I. Stolfa, S. Abreu, S. Mura, P. Chaminade, M. Espeli and E. Fattal, *J. Control. Release*, 2019, **296**, 179–189.
9 P. Beard, *Interface Focus*, 2011, **1**, 602–631.
10 J. P. Fuenzalida Werner, Y. Huang, K. Mishra, R. Janowski, P. Vetschera, C. Heichler, A. Chmyrov, C. Neufert, D. Niessing, V. Ntziachristos and A. C. Stiel, *Anal. Chem.*, 2020, **92**, 10717–10724.
11 T. Lucas, M. Sarkar, Y. Atlas, C. Linger, G. Renault, F. Gazeau and J. Gateau, *Sensors*, 2022, **22**, 6543.
12 J.-B. Bodin, J. Gateau, J. Coïs, T. Lucas, F. Lefebvre, L. Moine, M. Noiray, C. Cailleau, S. Denis, G. Clavier, N. Tsapis and R. Méallet-Renault, *ACS Appl. Mater. Interfaces*, 2022, 40501–40512.
13 J.-B. Bodin, C. Linger, J. Gateau, T. Beguin, T. Lucas, L. Moine, D. Chapron, M.-H. Ha-Thi, A. Fatima, G. Clavier, N. Tsapis and R. Méallet, *J. Phys. Chem. C*, 2023, Article ASAP.
14 K. Zlatić, H. B. E. Ayouchia, H. Anane, B. Mihaljević, N. Basarić and T. Rohand, *J. Photochem. Photobiol. A, Chem*, 2020, **388**, 112206.
15 J. L. Bricks, Y. L. Slominskii, I. D. Panas and A. P. Demchenko, *Methods Appl. Fluoresc.*, 2017, **6**, 012001.
16 H. Aoki, M. Nojiri, R. Mukai and S. Ito, *Nanoscale*, 2014, **7**, 337–343.